



A multiparametric volumetric quantitative ultrasound imaging technique for soft tissue characterization

Farah Deeba^{a,*}, Caitlin Schneider^a, Shahed Mohammed^a, Mohammad Honarvar^b, Julio Lobo^b, Edward Tam^c, Septimiu Salcudean^a, Robert Rohling^{a,d}

^a Department of Electrical and Computer Engineering, The University of British Columbia, Vancouver, Canada

^b Sonic Incytes, Vancouver, BC, Canada

^c LAIR Centre, Vancouver, Canada

^d Department of Mechanical Engineering, The University of British Columbia, Vancouver, Canada

ARTICLE INFO

Article history:

Received 29 March 2021

Revised 21 July 2021

Accepted 14 September 2021

Available online 24 September 2021

Keywords:

Quantitative ultrasound

Hepatic steatosis

Attenuation coefficient estimate

Backscatter coefficient

Effective scatterer diameter

ABSTRACT

Quantitative ultrasound (QUS) offers a non-invasive and objective way to quantify tissue health. We recently presented a spatially adaptive regularization method for reconstruction of a single QUS parameter, limited to a two dimensional region. That proof-of-concept study showed that regularization using homogeneity prior improves the fundamental precision-resolution trade-off in QUS estimation. Based on the weighted regularization scheme, we now present a multiparametric 3D weighted QUS (3D QUS) method, involving the reconstruction of three QUS parameters: attenuation coefficient estimate (ACE), integrated backscatter coefficient (IBC) and effective scatterer diameter (ESD). With the phantom studies, we demonstrate that our proposed method accurately reconstructs QUS parameters, resulting in high reconstruction contrast and therefore improved diagnostic utility. Additionally, the proposed method offers the ability to analyze the spatial distribution of QUS parameters in 3D, which allows for superior tissue characterization. We apply a three-dimensional total variation regularization method for the volumetric QUS reconstruction. The 3D regularization involving N planes results in a high QUS estimation precision, with an improvement of standard deviation over the theoretical $1/\sqrt{N}$ rate achievable by compounding N independent realizations. In the in vivo liver study, we demonstrate the advantage of adopting a multiparametric approach over the single parametric counterpart, where a simple quadratic discriminant classifier using feature combination of three QUS parameters was able to attain a perfect classification performance to distinguish between normal and fatty liver cases.

© 2021 The Authors. Published by Elsevier B.V.

This is an open access article under the CC BY-NC-ND license

(<http://creativecommons.org/licenses/by-nc-nd/4.0/>)

1. Introduction

The role of ultrasound, as a portable triage and monitoring tool, is becoming increasingly important, especially in the current context of a global pandemic. Conventional ultrasound images are formed from backscattered radio frequency echo signals created as a result of interaction with macro- and micro scale tissue structures. The B-mode image processing, including envelope detection

and log compression, highlights the large-scale ($>$ ultrasound wavelength) features such as the organ boundaries, while discarding the frequency-dependent smaller scale ($<$ ultrasound wavelength) structural information. The speckle pattern and echogenicity of the B-mode image, though related to the complex organization of smaller scale tissue structure and their averaging scattering strength, render the US imaging qualitative, system-dependent and open to user interpretation. Three decades of research in the field of quantitative ultrasound (QUS), followed by the pioneering works by Insana et al. (1990a) and Coleman and Lizzi (1983), established system and user independent techniques to quantify acoustic and microstructural properties by parametrizing the frequency dependent contents in the backscattered echo. Due to the reduced dependence on user interpretation as well as the efficacy for tissue typing and monitoring disease progression substantiated by extensive experimental research (Mamou and Oelze, 2013; Oelze and

Abbreviations: QUS, quantitative ultrasound; ACE, attenuation coefficient estimate; IBC, integrated backscatter coefficient; ESD, effective scatterer diameter; RPM, reference phantom method; TV, total variation; MRI-PDFF, magnetic resonance imaging proton density fat fraction; AUROC, area under the receiver operator characteristic curve.

* Corresponding author.

E-mail address: farahdeeba@ece.ubc.ca (F. Deeba).

Mamou, 2016), QUS imaging promises to further enhance the clinical utility of ultrasound.

Spectral based parametric imaging forms a major branch of QUS, which includes measurement of attenuation coefficient estimate (ACE), backscatter coefficient and scatterer properties such as effective scatterer diameter (ESD) and effective acoustic concentration (EAC) of scatterers. ACE is a frequency dependent acoustic property that measures the ultrasound energy loss with propagation depth due to the combined effect of scattering and absorption. Backscatter coefficient, on the hand, measures the ultrasound intensity that is scattered in the backward direction (normalized ultrasound backscattered power per unit volume of scatterers). The integrated backscatter coefficient (IBC) is a measure of the backscatter strength, which is estimated by integrating the backscatter coefficient in the effective frequency band of the transducer. Backscatter coefficient can further be used to estimate the ESD of the dominant sub-resolution ($<$ wavelength) scatterer, with the effective scale being determined by the incident ultrasound frequency. The spectral based QUS parameters have been successfully used in numerous clinical applications, including cancer detection in prostate and lymph nodes (Feleppa et al., 2011), bone health assessment (Laugier and Haiat, 2011), cervical ripening detection (Feltovich et al., 2012), breast lesion characterization (Nam et al., 2013), and placenta characterization (Deeba et al., 2019).

Liver steatosis quantification using QUS has undergone a recent surge in an effort to address the alarming increase in non-alcoholic fatty liver disease prevalence rate (25% globally) (Loomba and Sanyal, 2013). Previous works demonstrated that the cellular ballooning due to fat infiltration in the fatty liver affects the ultrasonic scattering process, resulting in an increase in ACE and Backscatter coefficient (Pohlhammer and O'Brien, 1980; Bamber and Hill, 1981). Several clinical studies on QUS showed promising results to quantify the fat content in liver, with efficacy comparable to magnetic resonance imaging proton density fat fraction (MRI-PDFF) and biopsy, the current gold standard for steatosis grading (Andre et al., 2014a; Lin et al., 2015; Fujiwara et al., 2018; Deeba et al., 2019b).

Current challenges towards the clinical translation of QUS imaging include large estimation bias and variance due to tissue inhomogeneity and precision-resolution trade-off (Liu et al., 2010; Oelze and O'Brien, 2004). The resolution-precision trade-off is particularly critical for thin (e.g. dermis) and heterogeneous (e.g. placenta) tissue characterization. Available smaller windows result in noisy power spectral estimates due to limited spectral resolution and spatial variation noise inherent in ultrasound scattering. Deviation from the homogeneity assumption arising from the variation in underlying scatterer statistics (Pawlicki and O'Brien, 2013), on the other hand, is likely to affect most biological tissue to different extent. Rubert et al. demonstrated that the high variance (with standard deviation being around 50% of the mean value) in ACE for *ex vivo* bovine liver is attributed to the deviation from the Rayleigh distribution, rather to the biological variability (Rubert and Varghese, 2014). A large variance due to spatial heterogeneity was also reported for a cervix remodelling assessment study, where the difference in QUS parameters between early and late pregnant cervix were obscured by the intra-class variation (McFarlin et al., 2015; Guerrero et al., 2018). The reliability of Controlled Attenuation Parameter (CAP, Fibroscan, Echosens, France), a promising commercial tool to detect and quantify hepatic steatosis, has been reported to be compromised due to the variability in attenuation estimates. For example, an IQR $>$ 40 dBm was found to be indicative of poor diagnostic accuracy (Wong et al., 2017).

Large axial window lengths and averaging over lateral and elevational RF lines reduce the spatial variation noise due to random scatterer positioning. These approaches offer improved accuracy and precision, assuming uniform scattering within inter-

rogated volume. Averaging also improves the power spectral estimation (Liu et al., 2010). Studies show that the Welch method, a refined periodogram that estimates the averaged periodogram of overlapped subwindows, was superior compared to rectangular, Hamming and Hanning windowing (Liu et al., 2010). While these techniques attain an improved estimation at the expense of spatial resolution, more recent works explore the possibility of extending the precision-resolution trade-off. Regularization incorporating a spatial prior was successful in simultaneously improving the resolution and the precision of QUS estimation for homogeneous regions (Coila and Lavarello, 2017a; Vajihhi et al., 2018; Rau et al., 2020). However, uniform regularization, which was used in Coila and Lavarello (2017a); Vajihhi et al. (2018); Rau et al. (2020), might not be appropriate for biological tissue with the presence of inhomogeneities, as it will lead to oversmoothing in homogeneous regions in an attempt to compensate for the local inhomogeneities. In our previous work, we presented a proof-of-concept study based on a spatially weighted total variation regularization method, where the adaptive regularization parameter was a function of local inhomogeneity (Deeba et al., 2019b). The study was limited to the measurement of a single QUS parameter, ACE, in a 2D region-of-interest and was validated using a small *in-vivo* liver study.

Another factor that might affect the clinical uptake of QUS imaging is the provision of visual guidance. CAP, which is performed in A-mode, lacks visual guidance, limiting ability to select the optimum region-of-interest. Several recent works on liver imaging have addressed the importance of B-mode and parametric image guidance to select an appropriate region-of-interest (ROI) that excludes vessels and extrahepatic areas (Fujiwara et al., 2018; Kanayama et al., 2013). 3D QUS imaging can further be advantageous over the 1-D or 2-D counterpart, allowing volumetric reconstruction, multimodal registration along with enhanced visualization and interpretation.

In this work, we present a multiparametric 3D weighted QUS (3D QUS) method using a 3D total variation regularization incorporating spatially variable regularization parameters. The proposed 3D adaptive total variation (TV) regularization exploits the spatial consistency information while preserving the variation in scattering properties in all three directions, thus would provide a rich spatial description of the tissue properties. The adaptive regularization is particularly important for QUS reconstruction in tissue regions with backscatter variation. We perform phantom validation, using phantoms with uniform and variable backscatter properties and demonstrate the superior QUS reconstruction performance of the proposed method compared to the baseline methods. Furthermore, the proposed method simultaneously generates multiple QUS maps, including ACE, IBC, and ESD, and therefore provides complementary information regarding the underlying tissue structure. The multiparametric approach could improve the class separability between normal and pathological tissue in the feature space. Toward this goal, we evaluate the benefit of a multiparametric approach over the single QUS counterpart in an *in vivo* liver study including healthy volunteers and patients with hepatic steatosis.

2. Methodology

2.1. 3D QUS: proposed volumetric quantitative ultrasound parameter estimation algorithm

In our previous work (Deeba et al., 2019b), we presented a single QUS parameter estimation method limited to a 2D region-of-interest. In the problem formulation, we utilized a simplified model for the backscatter coefficient, ignoring the frequency dependent term. Herein, we introduce a 3D multiparametric QUS

method, using an adaptive three-dimensional total variation regularization method (Section 2.1.1). As the adaptive regularization parameter, we utilize a 3D spatially weighted matrix as a function of envelope SNR (signal-to-noise ratio) deviation (Section 2.1.2). We further adopt an improved model of the backscatter coefficient considering its frequency dependence. Using this model, we formulate equations to extract scatterer statistics, such as effective scatterer diameter and effective acoustic concentration (Section 2.1.3).

2.1.1. Attenuation coefficient estimate and integrated backscatter coefficient measurement

A pulse-echo ultrasound system, with the assumption of weak scattering (i.e. the Born approximation) and negligible effect of diffraction and refraction, can be modeled as a simple frequency domain multiplication of pulse characteristics and backscatter characteristics (Trecee et al., 2005). The backscattered signal intensity, $S(f, z)$ obtained from a time-gated radio frequency signal window centered at depth z from the transducer surface at frequency f can be written as:

$$S(f, z) = G(f)A(f, z)B(f), \quad (1)$$

where $G(f)$ represents the transducer transfer function and transmit pulse. $A(f, z)$ represents the total attenuation effect from the transducer surface to the center of the respective time-gated window at depth z and $B(f)$ is the backscatter term. For most soft tissue, $A(f, z)$ is approximately linearly proportional to the frequency (Wear, 2002):

$$A(f, z) = e^{-4\alpha f z}, \quad (2)$$

where α (Np/cm/MHz) is the effective amplitude attenuation coefficient estimate for the round trip of the depth z .

The backscatter term, $B(f)$, in its simplest form, can be expressed as a scalar parameter, as has been adopted in the scattering model used by Field II (Jensen, 1996) and previous ACE computation works (Deeba, Schneider, Mohammed, Honarvar, Tam, Salcudean, Rohling, 2019, (Coila, Lavarello, 2017)). However, a more appropriate model is required to capture the non-linear frequency dependence of the BSC term (Trecee et al., 2005; Vajihhi et al., 2018):

$$B(f) = \beta f^n, \quad (3)$$

where β and n are backscatter parameters.

The reference phantom method (Yao et al., 1990), a widely adopted method for QUS estimation, removes the system dependence (e.g. cancels out the system dependent term, $G(f)$) by normalizing the signal intensity backscattered from the tissue sample utilizing the one obtained from a well-characterized reference phantom under the same transducer and system settings. Therefore, the ratio of the intensity backscattered from the tissue sample to that from the reference at (i, j, k) location at frequency f_p can be written as:

$$\begin{aligned} RS(f, z) &= \frac{S_s(f, z)}{S_r(f, z)} = \frac{A_s(f, z)B_s(f)}{A_r(f, z)B_r(f)} \\ &= \frac{\beta_s f^{n_s}}{\beta_r f^{n_r}} e^{-4(\alpha_s - \alpha_r) f z}, \end{aligned} \quad (4)$$

where s and r denote sample under experiment and the reference, respectively. Taking the natural logarithm of Eq. (4) leads to

$$\ln RS(f, z) = -4(\alpha_s - \alpha_r) f z + \ln \frac{\beta_s}{\beta_r} + (n_s - n_r) \ln f \quad (5)$$

Substituting the following variables in Eq. (5) as

$$\ln RS(f, z) = y, \quad 4fz = \phi, \quad \alpha_r - \alpha_s = \alpha, \quad \ln \frac{\beta_s}{\beta_r} = \beta, \quad n_s - n_r = n, \quad (6)$$

we obtain,

$$y = \phi \alpha + \beta + n \ln f \quad (7)$$

The system is defined in a $N_1 \times N_2 \times N_3$ ($N = N_1 N_2 N_3$) spatial grid and a frequency band discretized at M points is considered. We can represent the volumetric variables in vector format, for any variable $\mathbf{a} \in \mathbb{R}^N$ with elements $a_{i,j,k}$ ($i \in [1, N_1], j \in [1, N_2], k \in [1, N_3]$), reducing the forward model in Eq. (7) to

$$\mathbf{y} = \mathbf{A}\mathbf{x} + \mathcal{N}(0, \sigma_N), \quad (8)$$

where

$$\mathbf{A} = \begin{bmatrix} \phi_1 & \mathbf{I} & \ln f_1 \mathbf{I} \\ \phi_2 & \mathbf{I} & \ln f_2 \mathbf{I} \\ \vdots & \vdots & \vdots \\ \phi_M & \mathbf{I} & \ln f_M \mathbf{I} \end{bmatrix}, \quad \mathbf{y} = \begin{bmatrix} y_1 \\ y_2 \\ \vdots \\ y_M \end{bmatrix}, \quad \mathbf{x} = \begin{bmatrix} \alpha \\ \beta \\ n \end{bmatrix}.$$

Here, $\phi_m \in \mathbb{R}^{N \times N}$ is a diagonal matrix, with the diagonal elements evaluated at propagation depth $\mathbf{z} \in \mathbb{R}^N$ for frequency f_m ($m \in [1, M]$) is given by

$$\phi_m = 4f_m \text{diag}(\mathbf{z}). \quad (9)$$

The vector $\mathbf{y} \in \mathbb{R}^{NM}$ concatenates M sub-vectors $\mathbf{y}_m \in \mathbb{R}^N$, with each \mathbf{y}_m representing the volumetric power spectra ratio term evaluated at frequency f_m and $\mathbf{I} \in \mathbb{R}^{N \times N}$ is a identity matrix. $\mathcal{N}(0, \sigma_N)$ is the Gaussian noise present in the measurement of \mathbf{y} .

QUS parameters α , β , and n can abruptly change at the interface between two different tissue types, but these parameters will undergo gradual change (i.e. sparse spatial variation) within each tissue type. Therefore, with the piece-wise continuous assumption in all three spatial direction, we propose a 3D total variation regularization approach for the reconstruction of $\mathbf{x} = [\alpha, \beta, n]$ from the noisy estimation \mathbf{y} :

$$\hat{\mathbf{x}} = \arg \min_{\mathbf{x}} \|\mathbf{y} - \mathbf{A}\mathbf{x}\|_2^2 + \lambda_1 \|\alpha\|_{\text{TV}} + \lambda_2 \|\beta\|_{\text{TV}} + \lambda_3 \|n\|_{\text{TV}}, \quad (10)$$

where the first term is the data fidelity term, the last three terms are the anisotropic 3D total variation regularization terms, and λ_1 , λ_2 and λ_3 are the regularization weights.

The 3D spatially weighted TV regularizer for a variable η is defined as

$$\begin{aligned} \|\eta\|_{\text{TV}} &= \sum_{i,j,k} W_{i,j,k} \left(\frac{1}{(h_{i+1,i})_{jk}} |\eta_{i+1,j,k} - \eta_{i,j,k}| \right. \\ &\quad \left. + \frac{1}{(h_{j+1,j})_{ik}} |\eta_{i,j+1,k} - \eta_{i,j,k}| \right) + \frac{1}{(h_{k+1,k})_{ij}} |\eta_{i,j,k+1} - \eta_{i,j,k}| \end{aligned} \quad (11)$$

where the 3D weighted matrix $W_{i,j,k}$ is uniform for α , and spatially variable for β and n . $h_{i+1,i}$, $h_{j+1,j}$, $h_{k+1,k}$ are distances between the adjacent axial, lateral and elevational pixels respectively at corresponding spatial positions. The TV regularizer (Rudin et al., 1992) minimizes the sum of the gradients by imposing sparsity promoting l_1 -penalty in all three directions of the reconstructed QUS volume. By promoting signals with sparse gradients, TV minimization recovers piecewise-constant volumetric parameters.

Solving (10) and (6) will give the values of volumetric α_s , β_s and n_s . From the effective attenuation coefficient estimate, α obtained at depth z , the local attenuation coefficient estimate, α^{local} can be computed as:

$$\alpha_{i,j,k}^{local} = \frac{\alpha_{i,j,k} z_{i,j,k} - \alpha_{i-1,j,k} z_{i-1,j,k}}{z_{i,j,k} - z_{i-1,j,k}}.$$

The integrated backscatter coefficient (IBC) at (i, j, k) location can be computed as:

$$IBC = \frac{1}{f_M - f_1} \int_{f_1}^{f_M} \beta f^n df.$$

Table 1
Ground truth values for the phantoms.

Phantom		ACE (dB/cm/MHz)	IBC (dB)	ESD (μm)
Phantom 1	Zone 1	0.54	-28.60	51
	Zone 2	1.3	-29.96	51
Phantom 2	Background	0.84	-29.67	51
	Inclusion 1	0.37	-30.83	51
	Inclusion 2	0.74	-29.43	51
Phantom 3	Inclusion 3	1.18	-30.42	51
	Background	0.72	-35.40	90
	Inclusion 1	0.70	-35.11	342
	Inclusion 2	0.65	-31.01	158
	Inclusion 3	0.77	-28.72	51

2.1.2. Selection of the spatially weighted regularization parameter

Spectral-based methods, such as the reference phantom method, make the assumption that RF signal generation is a stationary scattering process, arising from a large number of randomly distributed scatterers identical in size. The RF envelope of such speckle pattern (namely fully developed speckle) can be modelled using the Rayleigh distribution (Goodman, 1985). There will be large measurement error and variance in QUS estimation when the underlying assumption for Rayleigh distribution is violated. Such conditions occur for ROIs with varying backscatter properties or finite scatterer density (< 10 scatterers per resolution cell) (Pawlicki and O'Brien, 2013; Rubert and Varghese, 2014). Therefore an adaptive regularization parameter is required, which is sensitive to the conditions leading to the underlying assumption for Rayleigh distribution.

Envelope SNR (SNR^{env}), defined as the ratio of the mean to the standard deviation of the RF signal envelope, is constant for a Rayleigh distribution and equals to $SNR^{opt} = 1.91$. The SNR^{env} value deviates from the Rayleigh level of 1.91 for conditions involving finite scatterer density (< 10 scatterers per resolution cell) or reduced degree of randomness (due to the presence of periodicity or clustering). Therefore, SNR^{env} can be used to identify media with low scatterer density, a source of large variance in ACE measurement (Rubert and Varghese, 2014). Though SNR^{env} cannot discriminate media with different backscatter characteristic for large scatterer densities (> 10 scatterers per resolution cell), it can identify the boundary of two such media, as the Rayleigh assumptions of identical diameter and random distribution do not hold at the boundary.

We define a normalized SNR^{env} parameter, envelope SNR deviation (ΔSNR^{env}) (Deeba et al., 2019), given at a spatial location (i, j, k) by

$$\Delta SNR_{i,j,k}^{env} = \frac{|SNR_{i,j,k}^{env} - SNR^{opt}|}{SNR^{opt}} \times 100\%. \quad (12)$$

Previous works qualitatively demonstrated the association between ΔSNR^{env} and backscatter variation from the visual inspection of inhomogeneity, lacking the quantitative description of BSC parameters (Deeba et al., 2019a,b). In this work, we investigate the dependence of ΔSNR^{env} on the quantitative backscatter parameters (i.e. IBC) and therefore validate the efficacy of ΔSNR^{env} to detect the backscatter variation within the Region-of-interest (ROI).

We perform a feasibility analysis on RF data acquired from a custom built ultrasound phantom (Table 1) with three inclusions of similar ACE and different backscatter characteristic, manufactured by CIRS (Norfolk, VA, USA). Inclusion 1 (with low scatterer density) can be identified from the background with significantly high ΔSNR^{env} , whereas inclusion 2 and inclusion 3 have similar ΔSNR^{env} as the background (Fig. 1 b). However, the boundaries for all three inclusions are highlighted with increased ΔSNR^{env} . This trend is also evident in the Rayleigh distribution fit to the RF envelope amplitude for selected ROIs, where the envelope amplitude

in the ROIs on the boundaries deviate from the Rayleigh distribution (Fig. 1 c). The spatial variation in ΔSNR^{env} correlates with the change in decibel scaled IBC (dB) (Fig. 1d). Therefore, ΔSNR^{env} is a suitable regularization parameter which can identify backscatter variation as well as sufficiently low scatterer density.

We propose a 3D spatially weighted matrix, $\{W_{i,j,k}\} \in \mathbb{R}^N$ as a function of ΔSNR^{env} to adaptively regularize the backscatter parameters, n and β :

$$W_{i,j,k}(\Delta SNR_{i,j,k}^{env}) = \frac{a}{1 + \exp[b \cdot (\Delta SNR_{i,j,k}^{env} - \Delta SNR_{min}^{env})]}, \quad (13)$$

where a and b are constants and ΔSNR_{min}^{env} is a nominal ΔSNR^{env} value for homogeneous region. For $\Delta SNR^{env} \ll \Delta SNR_{min}^{env}$, the weighting has little effect on the regularization. As the weight decreases with the increase in ΔSNR^{env} , the regularization effect on the backscatter terms is relaxed.

2.1.3. Effective scatterer diameter (ESD) measurement

The backscatter coefficient, when expressed in terms of an acoustic intensity form factor, can be used to extract the effective scatterer diameter (ESD) and effective acoustic concentration (EAC). We utilize a Gaussian form factor $F_{gauss} = \exp(-0.827k^2 a_{eff}^2)$ (Insana et al., 1990b), which assumes scattering sources with continuously varying acoustic properties randomly suspended in a fluid-like media. The backscatter coefficient, B can be written as:

$$B(f) = \frac{1}{9} k^4 a_{eff}^6 n \bar{\gamma}_0^2 F_{gauss}. \quad (14)$$

Here, $k = 2\pi f/c$ is the wave number, c is the sound speed, and a_{eff} is the effective scatterer radius. $n \bar{\gamma}_0^2$ is the net scattering strength, which is the product of the concentration of scatterers n times the relative impedance difference between the scatterers and surrounding tissues, $\bar{\gamma}_0^2$. $B(f) (= \beta f^n)$ is the backscatter coefficient measured using the 3D adaptive regularization method (Section 2.1.1).

Dividing by f^4 and then taking the natural logarithm on both sides of (14) we get:

$$\ln B_s(f) \cdot f^{-4} = \ln \left(\frac{1}{9} \left(\frac{2\pi}{c} \right)^4 a_{eff}^6 n \bar{\gamma}_0^2 \right) - 0.827 \left(\frac{2\pi f}{c} \right)^2 a_{eff}^2 \quad (15)$$

We can estimate a_{eff} and $n \bar{\gamma}_0^2$ by fitting a regression line, $y = mx + C$, where $y = \ln B_s(f) \cdot f^{-4}$, $x = f^2$, and

$$m = -0.827 \left(\frac{2\pi}{c} \right)^2 a_{eff}^2, \quad (16)$$

$$C = \ln \left(\frac{1}{9} \left(\frac{2\pi}{c} \right)^4 a_{eff}^6 n \bar{\gamma}_0^2 \right). \quad (17)$$

The effective scatterer diameter ($ESD = 2a_{eff}$) can be estimated from (16) and effective acoustic concentration ($EAC = 10 \log(n \bar{\gamma}_0^2)$) can be obtained solving (16) and (17) (Rohrbach et al., 2018). The 'Model Inversion' technique (Oelze et al., 2002) of measuring scattering properties by comparing measured backscatter spectrum to the theoretical one and fitting a regression line has been utilized in several previous works (Rohrbach et al., 2018; Nizam et al., 2020). This technique is computationally efficient over the traditional minimum average squared deviation (MASD) technique (Insana et al., 1990b). However, both of these techniques employ single time-gated window-based backscatter coefficient measures, which are prone to large measurement error. A previous work showed an improvement in QUS estimation using a nearest neighborhood averaging, which exploits the similarity among QUS measures of neighbouring windows (Nizam et al., 2020). In the proposed method, ESD is derived from a TV regularized backscatter

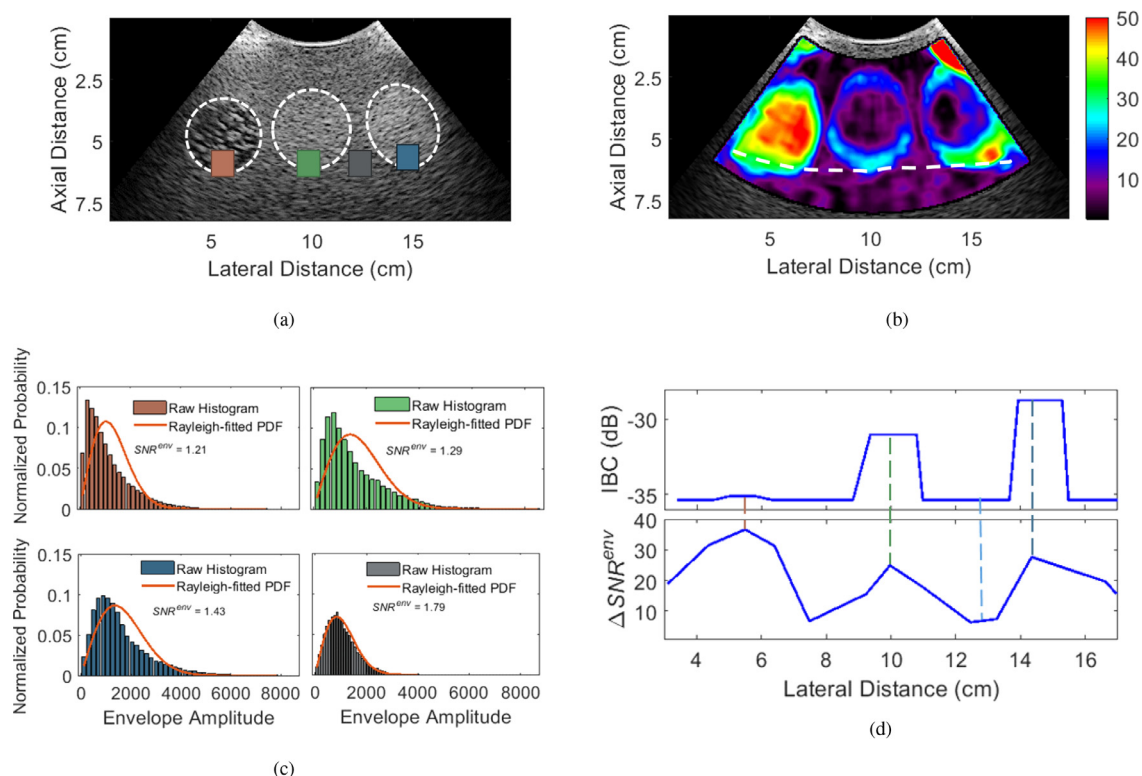


Fig. 1. Efficacy of the adaptive regularization parameter ΔSNR^{env} to identify BSC variation within the ROI. (a) B-mode image with dashed white line outlining the three inclusions. Four color-coded ROIs are selected at the boundaries of the inclusions and the background. Inclusion 1 - red, inclusion 2 - green, inclusion 3 - blue, and background - gray. (b) The adaptive regularization parameter ΔSNR^{env} map. (c) Rayleigh distribution fit associated to the selected ROIs. (d) IBC and ΔSNR^{env} along the curve shown in (b). The dashed lines correspond to the center point of the selected ROIs. (For interpretation of the references to color in this figure legend, the reader is referred to the web version of this article.)

measure and therefore exploits the sparse spatial variation of QUS parameters.

2.2. Data sets

2.2.1. Phantoms

The method was validated on three custom-built phantoms manufactured by CIRS (Norfolk, VA, USA). All three phantoms consisted of proprietary Zerdine hydrogel polymer and glass bead scatterers (Potter Industries, Malvern, PA, USA). Phantom 1 (as sketched in Fig. 2a) has two vertical homogeneous zones with similar backscatter properties and variable ACE. Zone 1 of phantom 1 is used as the reference phantom. Phantom 2 and phantom 3 (sketched in Fig. 2b) both include three spherical inclusions. The acoustic properties within the inclusion and the background were adjusted by adding soda lime glass microspheres (Spherglass®, Potters Industries Inc., PA, USA) of varying diameter and concentration. The inclusions in phantom 2 have variable ACE properties and similar backscatter and scatterer size properties, whereas the inclusions in phantom 3 have similar ACE with variable backscatter and scatterer size properties. The ground truth values for the QUS parameters reported by CIRS have been listed in Table 1. For all the experiments, zone 1 of phantom 1 was used as the reference phantom.

2.2.2. In vivo liver

A cross-sectional study was performed, which included a cohort of twenty-one adult participants, with 13 healthy controls (defined as MRI-PDFF < 5%) and 8 NAFLD patients (MRI-PDFF > 5%). This study (H14-01964) was performed under written informed consent after approval by the UBC Clinical Research Ethics Board. All

the participants underwent MRI and ultrasound examination between May 2017 and May 2018. MRI was performed on a 3.0 T system (Philips Achieva, Philips Medical Systems) with a dual-echo (DDE) sequence (Mashhood et al., 2013), where images are acquired in two dual-echo sequences at three time-points corresponding to nominal out-of-phase and in phase time (images at first in-phase time are acquired in both sequences). The first sequence acquires two images at sequential echo times of 1.15/2.3 msec and the second sequence acquires two more images at sequential echo times of 2.3/4.6 msec. A three-point Dixon method was used to determine the MRI-PDFF (proton density fat fraction). MRI-PDFF computed from the MRI data has been found to be strongly correlated with histological steatosis grading (Noureddin et al., 2013). Therefore, MRI-PDFF was used as a gold standard for hepatic steatosis detection, where an MRI-PDFF > 5% was defined as presence of hepatic steatosis. The ultrasound data were acquired from the right lateral intercostal window of the volunteer, laid in a supine position on a shaker board propagating the mechanical excitation.

2.3. Data acquisition and processing

2.3.1. 3D QUS method overview

The proposed volumetric QUS imaging technique was implemented on a standard 3D ultrasound system, which comprises an Ultrasonix SonixTouch ultrasound machine (Analogic, Richmond, BC, Canada), and a m4DC7-3/40 4D transducer. The transducer center transmit frequency was set to 3.33 MHz whereas the imaging depth was set to 15 cm with a focus at 13 cm. The customized motor control module allows the acquisition of volumetric RF data consisting of 15 planes spaced at 1° angular distance, with 25 frames acquired at each plane location at an effective frame rate

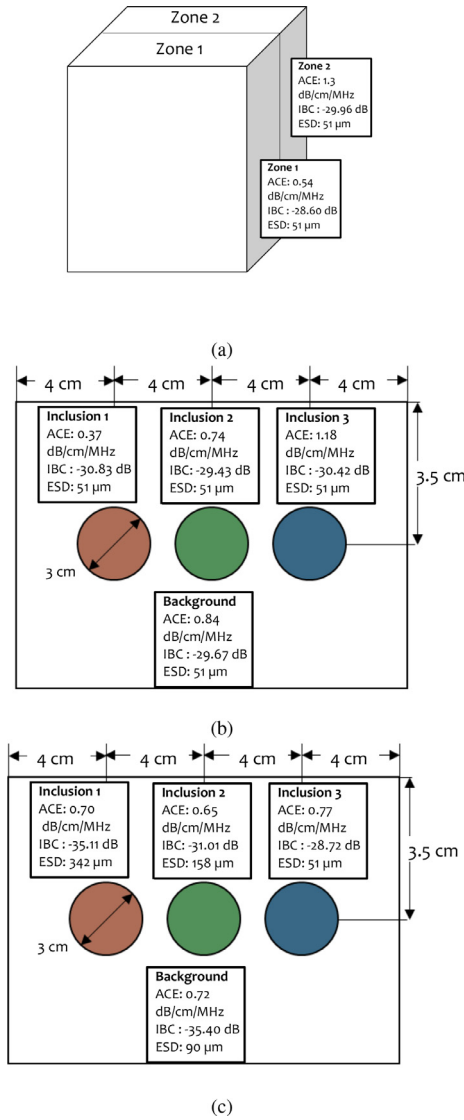


Fig. 2. Diagram of the custom-made CIRS phantoms.(a) Phantom 1 with two vertical layers; and (b) phantom 2 with three spherical inclusions (variable ACE and similar backscatter (IBC) and scatterer diameter (ESD) property) and (c) phantom 3 with three spherical inclusions (similar ACE and variable backscatter (IBC) and scatterer diameter (ESD) property).

of 250 frame-per-second (fps). Each 2-D frame in the 3-D volume consists of 64 RF scanlines covering a lateral field-of-view of 79°. The sampling rate was 20 MHz, resulting in 3870 samples in each scanline.

2.3.2. RF data processing and analysis

The proposed method was implemented in MATLAB 2018a (The MathWorks Inc., Natick, MA, USA). The optimization problem was solved using the convex optimization toolbox CVX in MATLAB (Grant et al., 2009). We compare the performance of the proposed 3D QUS method against the baseline reference phantom method (RPM) and a uniform 2D QUS method utilizing 2D uniform total variation regularization (Coila and Lavarello, 2017a), applied on each of the elevational planes separately.

We manually selected ROIs within the tissue or phantom, excluding the near-field data suffering from ringdown and other artifacts associated with transducer-to-phantom interface. Each ROI included 25 temporal frames. Each frame within the ROIs were divided into time-gated windows with 80% overlap in both lateral

and axial direction. The optimum dimensions for the time-gated windows for RPM were found to be 20 scan lines laterally and 50 wavelength (λ) (600 samples or 2.3 cm) axially. Here, the axial extent of one wavelength is approximately 0.46 mm. On the other hand, the dimensions for the time-gated windows for the regularization methods were selected as 5 scanlines laterally and 1.2 cm (300 samples or 25 λ) axially. The Welch method (Welch, 1967) was used to obtain the power spectrum from the RF scan lines within each time-gated window. We considered the -20 dB bandwidth of the received power spectrum as the usable frequency range.

The power spectra obtained from a single realization suffers from large variance due to statistical fluctuations arising from a random media. Compounding n statistically independent but equivalent realizations have been found to improve the power spectral estimate by reducing the standard deviation proportional to $1/\sqrt{n}$. Previously, different spatial and angular compounding based on spatial translations or rotations have been adopted to decorrelate the signal allowing independent realizations of RF data (Li and Odonnell, 1994; Gerig et al., 2004; Herd et al., 2012). In the proposed method, we perform averaging of the periodograms spatially and temporally, using 5 lateral scanlines and 25 temporal frames, to compute the power spectral density. To further improve the QUS estimation using RPM, we average the periodograms over the elevational planes resulting in a single QUS plane. The 2D QUS method applies 2D uniform regularization on each of the elevational planes separately, whereas the 3D QUS method applies 3D adaptive regularization using all the elevational planes. Specifically, the use of RF data from different elevational planes in 3D QUS allows independent realizations of signal data to be averaged. Several previous studies have utilized the correlation coefficient to measure the degree of change in the speckle pattern between different realizations, and consequently the effectiveness of ultrasound compounding (Herd et al., 2012; Rosado-Mendez et al., 2013; Liu et al., 2010). We compute the correlation, ρ between two planes separated by ΔN planes:

$$\rho(\Delta N) = \frac{\sum_{i=1}^{N_1} \sum_{j=1}^{N_2} (X_{i,j,k} - \bar{X}_k)(X_{i,j,k+\Delta N} - \bar{X}_{k+\Delta N})}{\sqrt{\sum_{i=1}^{N_1} \sum_{j=1}^{N_2} (X_{i,j,k} - \bar{X}_k)^2 (X_{i,j,k+\Delta N} - \bar{X}_{k+\Delta N})^2}},$$

where $X_{i,j,k}$ denotes the i th axial RF data point of the j th scanline in the k th plane for a volume-of-interest with N_1 , N_2 and N_3 data points in the axial, lateral and elevational directions, respectively. Two planes, for which the correlation is low (< 0.2), are considered to be sufficiently independent required for improving QUS estimation precision (Herd et al., 2012; Rosado-Mendez et al., 2013).

The initial guesses for parameters a and b in Eq. (13) were determined as follows: first we plotted the IBC error for phantom 3 (similar ACE and variable IBC) as a function of ΔSNR^{env} and fit a curve with an equation form given in Eq. (13). The curve fitting gives an estimate of the parameters a and b , which were further tuned to match the ground truth QUS values of the phantoms. We tune the regularization weights λ_1 , λ_2 and λ_3 to obtain optimum QUS reconstruction results for the homogeneous phantom (phantom 1) and the variable ACE phantom (phantom 2). The regularization weights used for all QUS results presented in this paper using the 2D QUS method were $\lambda_1 = 2^0$, $\lambda_2 = 2^{-2}$, $\lambda_3 = 2^{-3}$, whereas $\lambda_1 = 2^{0.5}$, $\lambda_2 = 2^0$, $\lambda_3 = 2^{-0.5}$ were used for the 3D QUS method. Also, we empirically select $a = \text{mean}(\Delta SNR^{env})$ and $b = 0.09$ in Eq. (13) for all experiments in this paper.

2.4. Evaluation metrics

The mean and standard deviation of ACE, IBC and ESD were measured and reported. The accuracy and precision were assessed using the mean absolute percentage error and standard deviation

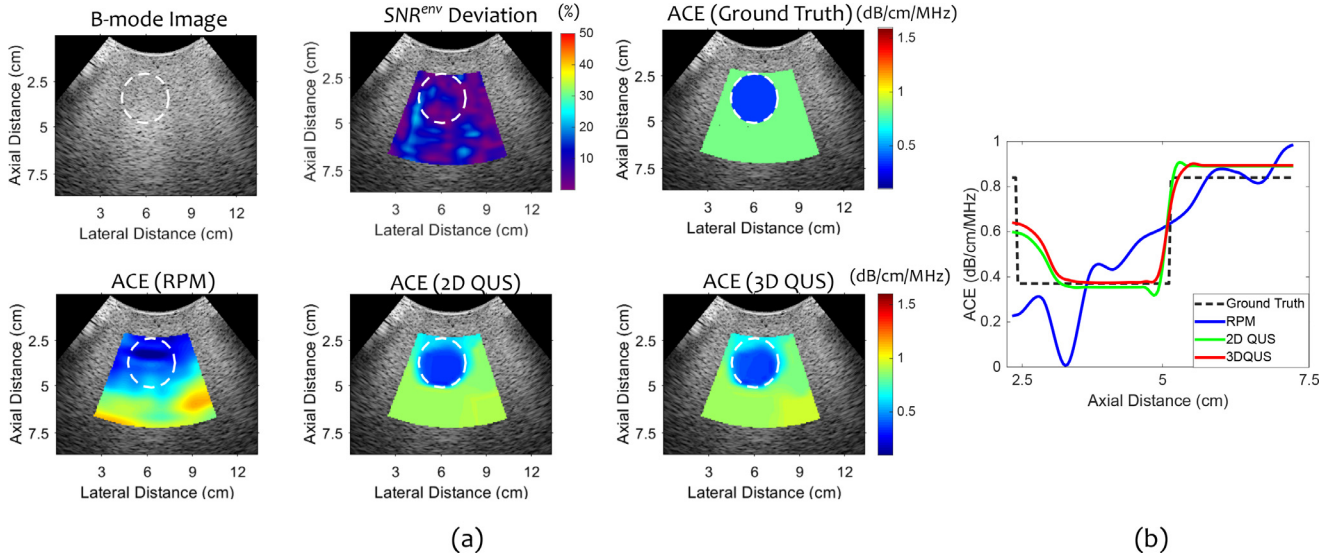


Fig. 3. (a) ΔSNR^{env} map, ground truth ACE map and reconstructed ACE map using different methods for inclusion 1 in phantom 2 (variable ACE and approximately uniform backscatter and scatterer size property) and (b) the profile of the reconstructed ACE along the axially central line through the inclusion.

of absolute percentage error, respectively. Absolute percentage error of a quantity $\mathbf{a} \in \mathbb{R}^N$, is defined as:

$$APE = \frac{|\mathbf{a}_{estimated} - \mathbf{a}_{actual}|}{\mathbf{a}_{actual}} \times 100\%, \quad (18)$$

where APE is the absolute percentage error, $\mathbf{a}_{estimated}$ and \mathbf{a}_{actual} represent the reconstructed and the ground truth measure of a QUS quantity, respectively.

The detectability of an inclusion in a QUS map was evaluated using contrast-to-noise ratio (CNR) ratio:

$$CNR = \frac{|\mu_{inc} - \mu_{bg}|}{\sqrt{\sigma_{inc}^2 + \sigma_{bg}^2}}, \quad (19)$$

where μ and σ are the mean and standard deviation of a QUS quantity within the inclusion and the background denoted by the subscripts *inc* and *bg*, respectively. The inclusions were delineated from the B-mode images, refined using the position and dimension information provided by the manufacturer.

To evaluate steatosis detection performance for in vivo liver, the correlation between MRI-PDF and QUS measures were calculated using Spearman's rank correlation coefficient. Also, the classification accuracy and the area under the ROC curve (AUROC) were measured to evaluate the classification performance using different combination of QUS parameters.

3. Experiments and results

3.1. Phantom validation

The ACE reconstruction results for phantom 2 (variable ACE and similar backscatter and scatterer size properties) are shown in Fig. 3. From the ΔSNR^{env} map, it is evident that the variation in ACE does not cause deviation of SNR^{env} values from SNR^{opt} . With $\Delta SNR^{env} < \Delta SNR_{min}^{env}$, the spatial weighting has little effect on the regularization. Therefore, QUS reconstruction results from the 2D QUS method with uniform regularization and the 3D QUS with adaptive regularization are similar, where both methods clearly identify the low attenuation inclusion from the high attenuation background. The RPM, on the other hand, detects the variation in ACE with a poorer resolution compared to the regularization methods.

Fig. 4 shows the results for phantom 3 (approximately uniform ACE and variable backscatter and scatterer size properties). As previously discussed in Section 2.1.2, the variation in backscatter characteristic is associated with a variation in ΔSNR^{env} map. The 3D QUS method, that incorporates the ΔSNR^{env} information for enabling adaptive regularization, yields more accurate reconstruction of the IBC map compared to its uniform regularization counterpart, 2D QUS (Fig. 4(a)). The RPM failed to generate a reasonable IBC result. The ACE maps obtained from the three methods have also been shown in Fig. 4(c). Both the RPM and the 2D QUS method exhibit consecutive undershoot and overshoot in ACE measurement at the boundary between medium with different backscatter properties, a trend described in previous literature (Pawlicki and O'Brien, 2013; Deeba et al., 2019b). The proposed 3D QUS method, on the contrary, was able to overcome the issue, yielding accurate ACE results.

The ESD map for phantom 3 has been shown in Fig. 5. The RPM and the 2D QUS method using uniform regularization were not successful to reconstruct the ESD map, as were expected from the inaccurate estimation of IBC map. The proposed 3D QUS method results in improved ESD reconstruction.

For the quantitative comparison of the QUS parameters, we compare the mean and standard deviation of the ACE in phantom 2 and IBC and ESD in phantom 3 for the inclusions and the background. For IBC, we compute the standard deviation of the IBC error expressed in dB. The results are shown in Fig. 6.

We also report the mean absolute percentage error and standard deviation of absolute percentage error results in Tables 2 and 3. We include the results obtained using 2D adaptive QUS along with 2D QUS and 3D QUS to highlight the effect of 3D regularization compared to the 2D regularization and adaptive regularization compared to the uniform regularization. In case of ACE, both the 2D QUS method and the 3D QUS method reach close to the ground truth value with high precision with mean and standard deviation of absolute percentage error below 10%, enabling accurate ACE characterization. However, for IBC and ESD estimation, the proposed 3D QUS method consistently outperforms the other methods, where the mean absolute percentage error in IBC remained below 25% and standard deviation of absolute percentage error in IBC was below 11% for 3D QUS. 2D adaptive QUS yield improved result compared to its uniform counterpart (2D QUS), however, was outperformed by the 3D counterpart (3D QUS).

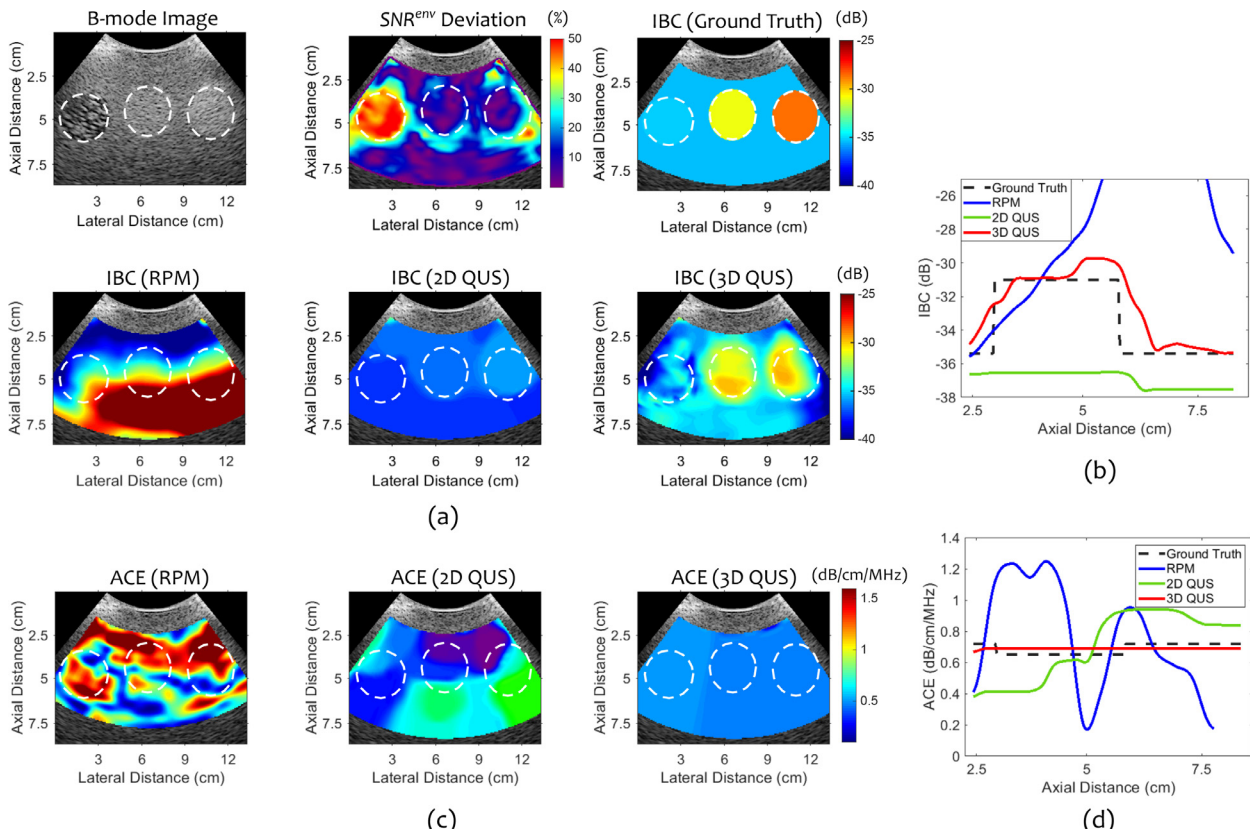


Fig. 4. (a) ΔSNR^{ENV} map, ground truth IBC map and reconstructed IBC maps using different methods for phantom 3 (similar ACE and variable backscatter and scatterer size property). Inclusion 1, 2, and 3 have been annotated in all the maps. (b) The profile of the reconstructed IBC along the axial central line through inclusion 2. (c) Reconstructed ACE maps using different methods for phantom 3 and (d) the profile of the reconstructed ACE along the axial central line through inclusion 2.

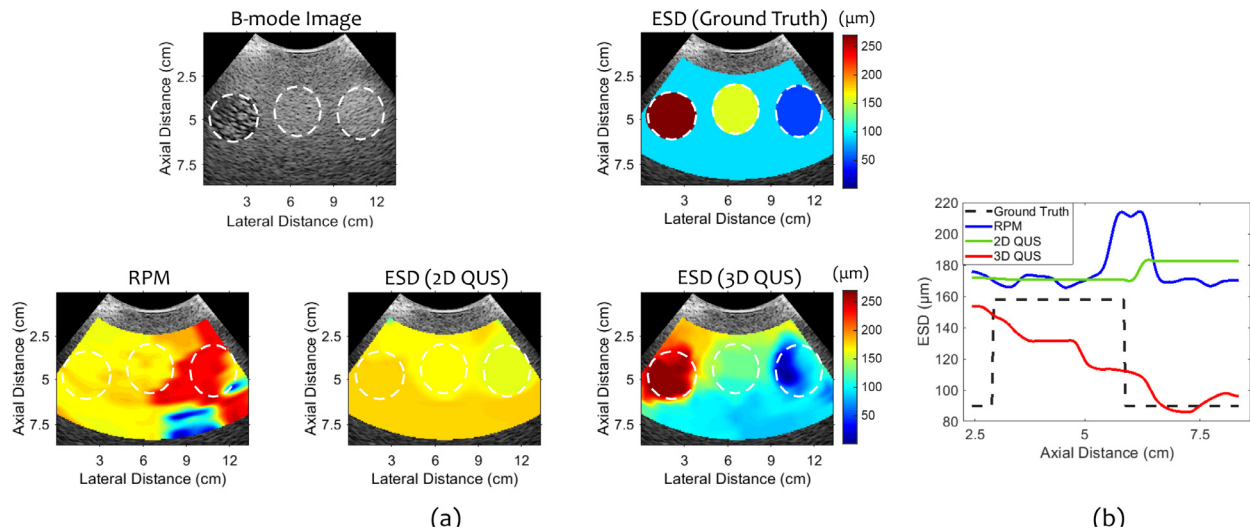


Fig. 5. (a) ΔSNR^{ENV} map and reconstructed ESD maps using different methods for phantom 3 (approximately uniform ACE and variable backscatter and scatterer size property) with inclusion 1, 2, and 3. (b) The profile of the reconstructed ESD along the axial central line through inclusion 2.

We evaluate the CNR of the QUS parameters for different methods. Fig. 7 shows the mean and standard deviation computed over the three inclusions in respective phantom. The mean CNR values obtained using the proposed 3D QUS method were larger than the other two methods. Compared to the baseline RPM, the 3D QUS method results in around 4.2 fold, 1.8 fold and 2.9 fold increase in the CNR for ACE, IBC, and ESD, respectively. Also, the 3D QUS improves the CNR by 1.4 times and 1.9 times compared to the 2D QUS method (uniform regularization) for IBC and ESD, respectively.

3.2. Effect of compounding using three-dimensional regularization

Unlike conventional QUS method, we acquire multiple elevational planes of RF data in the proposed method. We perform a three-dimensional adaptive TV regularization to obtain the volumetric QUS maps. Previous studies used different ultrasound compounding techniques, such as angular compounding and deformation compounding to reduce the standard deviation in QUS estimation, such as scatterer size [3] and backscatter coefficient [4]. To study the effect of the proposed compounding using three di-

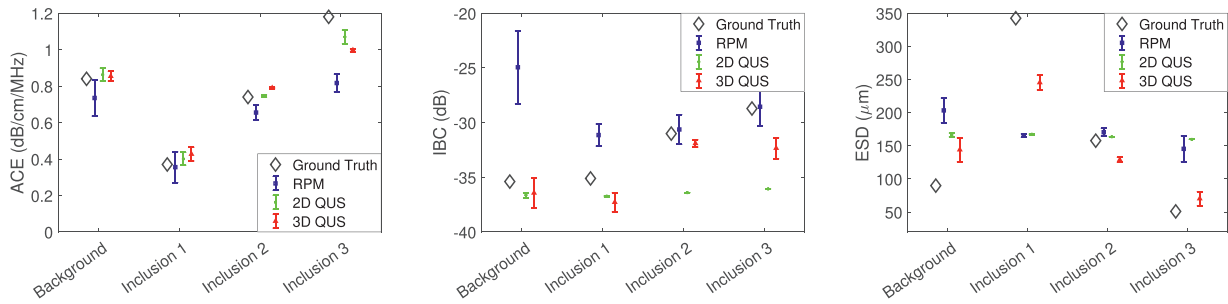


Fig. 6. Mean and standard deviation of ACE in phantom 2 (left), IBC (middle) and ESD (right) in phantom 3 using different methods.

Table 2

Estimated mean and standard deviation of absolute percentage error for the reconstructed ACE and IBC maps for the experimental phantoms.

Phantom	ACE (dB/cm/MHz)							
	Mean absolute percentage error (%)				Std. of absolute percentage error (%)			
	RPM	2D QUS	2D adaptive QUS	3D QUS	RPM	2D QUS	2D adaptive QUS	3D QUS
1	7.43	2.97	4.34	2.96	4.61	0.35	0.80	0.71
2	23.05	8.23	10.62	9.68	16.75	6.77	6.92	6.06
3	61.15	19.93	9.61	7.34	37.52	8.90	0.65	2.3e-6
Phantom	IBC (dB)							
	Mean absolute percentage error (%)				Std. of absolute percentage error (%)			
	RPM	2D QUS	2D adaptive QUS	3D QUS	RPM	2D QUS	2D adaptive QUS	3D QUS
1	6.30	24.94	9.45	23.29	3.55	3.61	5.83	0.37
2	135.97	34.15	20.72	24.15	125.17	7.39	12.60	10.66
3	2247.2	64.11	31.69	22.83	866.25	2.42	9.73	10.48

Table 3

Estimated mean and standard deviation of absolute percentage error for the reconstructed ESD map for phantom 3.

Region	Mean absolute percentage error (%)				Standard deviation of absolute percentage error (%)			
	RPM	2D QUS	2D adaptive QUS	3D QUS	RPM	2D QUS	2D adaptive QUS	3D QUS
Inclusion 1	51.71	51.14	46.62	28.35	1.56	0.34	3.85	6.44
Inclusion 2	8.11	3.78	32.38	18.36	7.36	0.62	6.42	4.78
Inclusion 3	192.18	213.16	106.09	45.08	55.81	0.19	65.02	33.80
Background	154.76	111.19	82.02	30.95	36.58	11.24	32.53	40.32

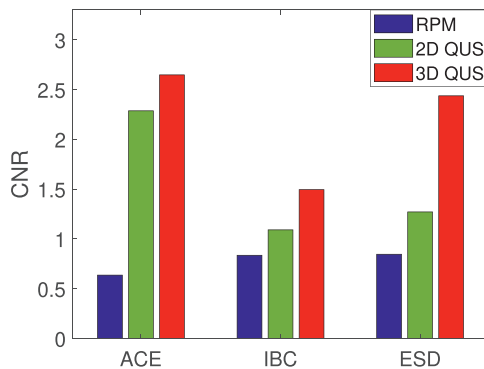


Fig. 7. CNR for ACE, IBC and ESD measures obtained from different methods.

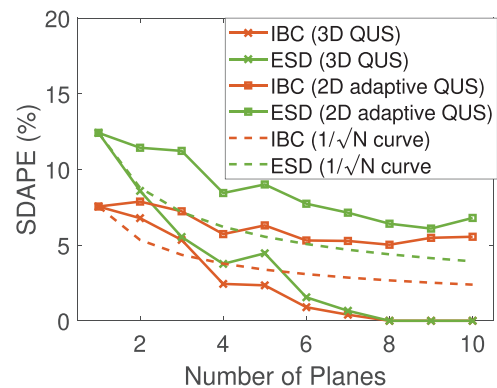


Fig. 8. Standard deviation of absolute percentage error in IBC and ESD measure obtained using three-dimensional TV regularization and two-dimensional TV regularization vs. the number of planes used in the computation. The dashed lines represent the theoretical $1/\sqrt{N}$ curves obtained by averaging N completely uncorrelated planes.

dimensional regularization, we vary the number of planes and evaluate the precision by computing standard deviation of absolute percentage error for ACE, IBC and ESD measures. We also investigate whether compounding obtained by three dimensional regularization has any advantage over the two-dimensional counterpart, two-dimensional regularization followed by averaging over elevational planes). Therefore, we perform 2-dimensional adaptive regularization after averaging the estimated power spectra from multiple planes. The results have been shown in Fig. 8. Also, the $1/\sqrt{N}$

curves for IBC and ESD have been superimposed on the graphs, where N represents the number of planes used in the computation. For uncorrelated planes, the standard deviation of absolute percentage error curves theoretically follow the $1/\sqrt{N}$ curve. The ACE variance remains unaffected (standard deviation of absolute

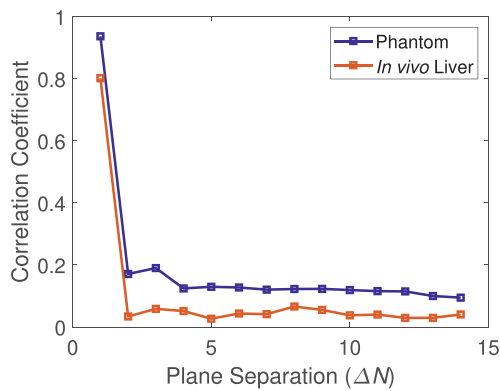


Fig. 9. Correlation coefficient between two 2-D radio-frequency (RF) signals separated by ΔN planes for a phantom and an in vivo liver example.

percentage error $< 0.5\%$) as the number of planes increases for this particular example of homogeneous phantom. For IBC and ESD measures, increasing the number of planes improve the estimation variance for compounding elevational planes using both 2D and 3D regularization methods. However, the compounding using 3D regularization not only outperforms the 2D regularization estimation precision, but the reduction in standard deviation of absolute percentage error measure improves over the $1/\sqrt{N}$ rate, which is the theoretical rate obtained by averaging N uncorrelated realizations.

Fig. 9 shows that the radio-frequency data in subsequent elevational planes obtained from in vivo liver are more decorrelated compared to the one obtained from the phantom. Improvement in QUS precision requires compounding of independent realizations. Ultrasound planes are considered to be sufficiently independent when the corresponding correlation is low (< 0.2) (Herd et al., 2012; Rosado-Mendez et al., 2013). Therefore, the improved decorrelation between subsequent planes is an effective indicator of improvement in QUS measurement for in vivo liver compared to phantom.

3.3. Effect of spatial weighting in total variation regularization

The phantom study demonstrates that the spatial weighting in the proposed 3D QUS method improves the QUS estimation, even in regions with high backscatter variation. In this section, we investigate the effect of spatial weighting on the selection of regularization parameter and QUS estimation performance. In 10(a) and (b), we compare the cost function value for different values of regularization parameters obtained at the ground truth QUS measures for the 3D adaptive QUS and 2D uniform QUS method. As it is difficult to visualize a 4-dimensional cost function, we set the values of λ_2 and λ_3 equal. We found that the spatial weighting keeps the optimum cost comparatively less variable for different λ_2 and λ_3 values for variable ACE region-of-interest (homogeneous as dictated by low ΔSNR^{env}). The effect is more pronounced for phantom 3 with variable backscatter property (high ΔSNR^{env}).

Fig. 10(c) demonstrates that the error in QUS parameter estimation can be optimized by choosing a suitable regularization parameter set for both the 3D QUS and the 2D QUS method. However, for the 3D QUS, the optimum ranges for regularization parameter coincide, whereas for the 2D QUS with uniform regularization, the ranges do not overlap. Therefore, it is possible to select an optimum regularization parameter for the 3D QUS method to optimize QUS parameter estimation irrespective of homogeneity (backscatter variation). On the contrary, the 2D QUS with uniform regularization would require different parameters set depending on the underlying tissue characteristic, which would not be feasible for clinical application.

3.4. In vivo liver: steatosis detection performance

The correlation results between MRI-PDFF and QUS measures have been displayed in Fig. 11. The ACE and IBC measures demonstrated significant positive associations with MRI-PDFF, whereas ESD was negatively associated to MRI-PDFF. The proposed 3D QUS method yields stronger correlation between ACE and MRI-PDFF ($r = 0.877$, $p < 0.001$) compared to the RPM ($r = 0.415$, $p = 0.062$) and the 2D QUS ($r = 0.645$, $p = 0.002$) method. The IBC measure had similar and significantly strong association with MRI-PDFF for both the 2D QUS ($r = 0.914$, $p < 0.001$) and the 3D QUS method ($r = 0.912$, $p = 0.004$) and a moderate correlation for the RPM ($r = 0.602$, $p < 0.001$). On the other hand, the 2D QUS ($r = -0.731$, $p < 0.001$) and 3D QUS method ($r = -0.51$, $p = 0.02$) yield strong to moderate negative association, whereas the noisy ESD results obtained by the RPM ($r = -0.265$, $p = 0.53$) almost obscures the correlation.

From the correlation analysis, the 2D QUS and the 3D QUS method exhibit comparable performance. However, a feature analysis plot including all three QUS features in Fig. 12 shows that the 3D QUS results in an improved separability between the steatosis and non-steatosis group compared to the 2D QUS method.

We utilize a quadratic discriminant analysis (QDA) classification to classify the cases into steatosis and non-steatosis group. The classification accuracy, the area under the ROC curve (AUROC) and the pair-wise p value of the difference between the AUROC measures (DeLong et al., 1988) from 2D QUS and 3D QUS were reported in Table 4. IBC, as a single feature, exhibits superior ability to discriminate while using the regularization methods: 2D QUS and 3D QUS, with AUROC close to 1 and statistically significant ($p < 0.05$) improvement compared to the RPM. Among different feature combination, ACE and IBC, ACE and ESD, and all three feature combination yield comparable performance, for which AUROC were significantly different compared to the one obtained from RPM. Compared to 2D QUS, 3D QUS yields better accuracy and AUROC for all feature combinations, which were, however, not statistically significant, except the case for ACE.

4. Discussion

Adopting a total variation regularization scheme extends the trade-off between estimation accuracy, precision, and spatial resolution. A window dimension of 30 scanlines (10 uncorrelated scanlines) and 35λ (13 pulse lengths) was found to be the minimum reliable dimension without incorporating regularization. This findings lie within the range of 7–15 pulse lengths and 10–20 uncorrelated scanlines, which are presented as the dimensions offering the best trade-off between spatial resolution, accuracy, and precision (Rosado-Mendez et al., 2013) for QUS estimation. In contrast, incorporating the total variation regularization into the 2D and the 3D QUS methods results in a dramatic improvement in precision of both ACE and IBC, where standard deviation of absolute percentage error remains below 5% for a window dimension of 10λ (≈ 3.75 pulse lengths) and 25λ (≈ 9.40 pulse lengths) axially and 5 (≈ 2 uncorrelated) scanlines, laterally. The mean of the absolute error of ACE and IBC remained below 6% and 40%, respectively for both the regularization methods. We can compare the accuracy performance with the previous work (Vajihhi et al., 2018) using a regularization method, which was able to achieve a mean percentage error (MPE) of 0.46% in ACE and 327% MPE and 19.7% MPE in estimation of backscatter parameters, b and n . Our results remain consistent with the previous studies (Wear et al., 2005), where backscatter estimations have been found to suffer from significant measurement error, ranging within 2 orders of magnitude.

Both 2D QUS and 3D QUS methods yield similar performance for the homogeneous phantom (phantom 1) and variable ACE

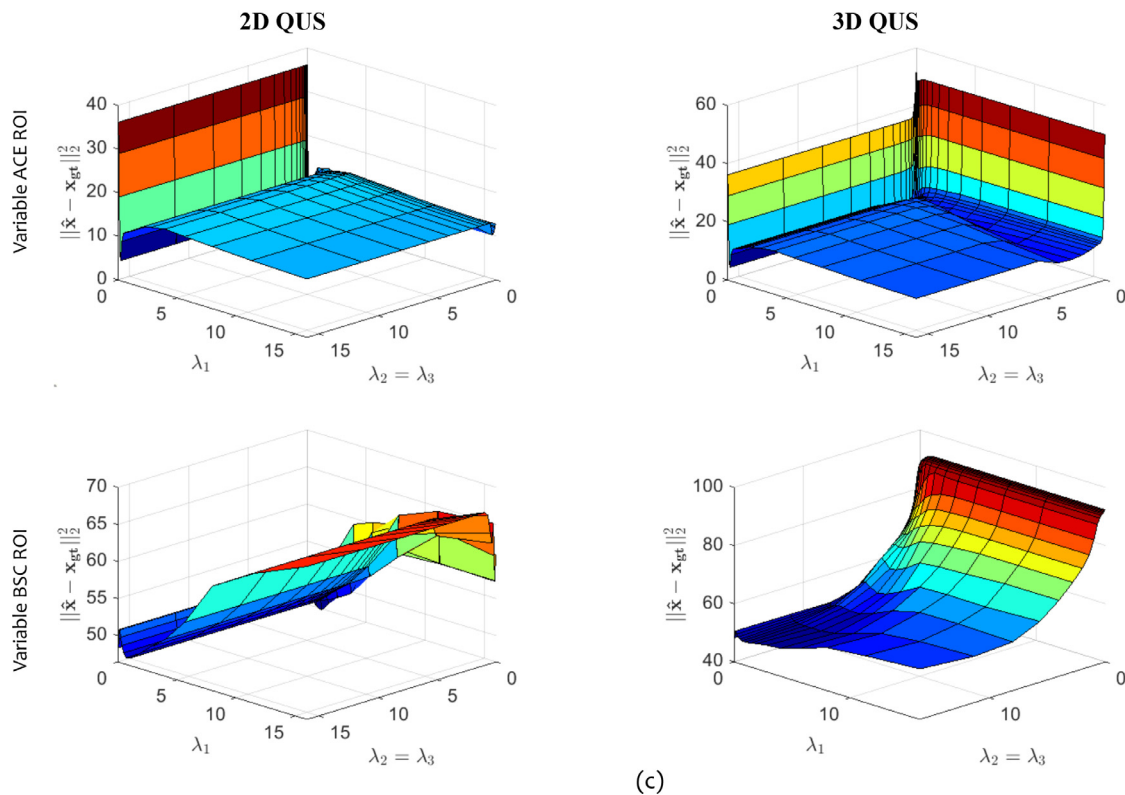
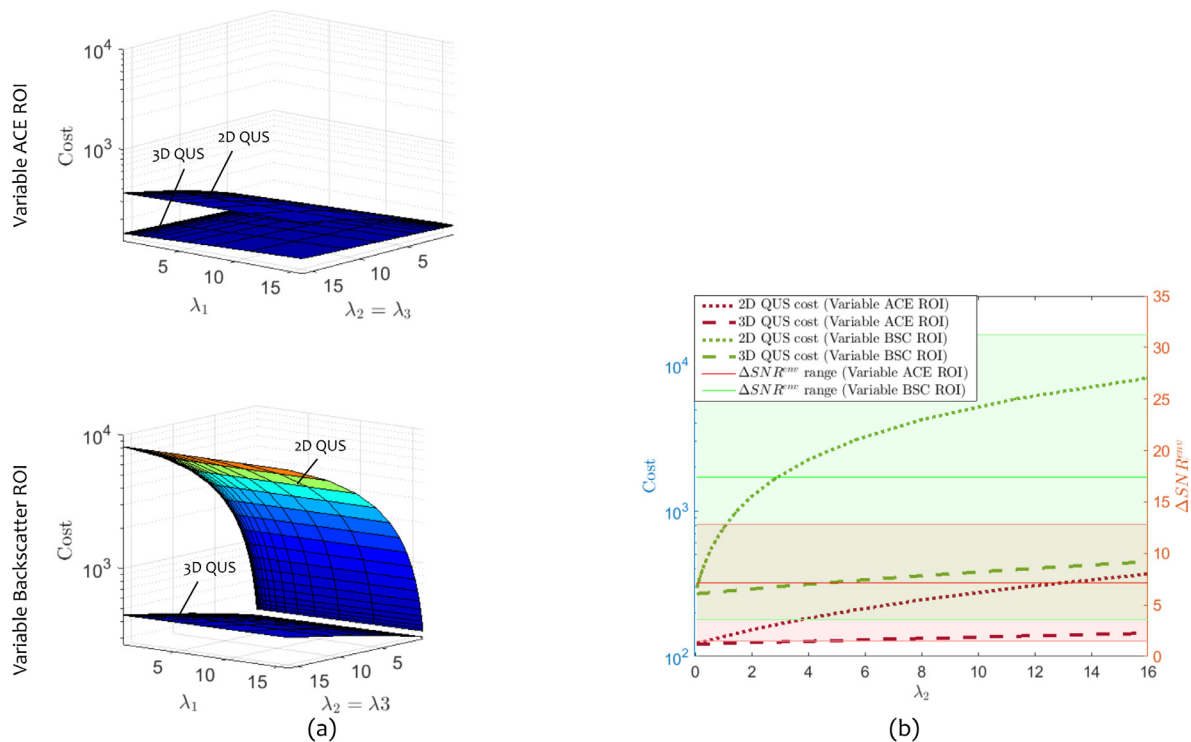


Fig. 10. Effect of spatial weighting using phantom 2 (variable ACE) and phantom 3 (variable backscatter and scatterer diameter property). (a) Cost evaluated at ground truth values of QUS parameters using the 2D QUS and the 3D QUS for different values of regularization parameters, λ_1 , λ_2 and λ_3 . For both cases, the upper surface is obtained from the 2D QUS and the lower one is from the 3D QUS. (b) Cost evaluated at ground truth values using the 2D QUS and the 3D QUS for different values of regularization parameter, λ_2 , when $\lambda_1 = 2^{-4}$ and $\lambda_3 = \lambda_2$. The shaded regions indicate the range of ΔSNR^{mv} , where the mid line is the mean ΔSNR^{mv} and the upper and lower lines are the standard deviation. (c) Error in QUS parameters estimation resulted from the 2D QUS and the 3D QUS for different values of regularization parameters, λ_1 , λ_2 and λ_3 .

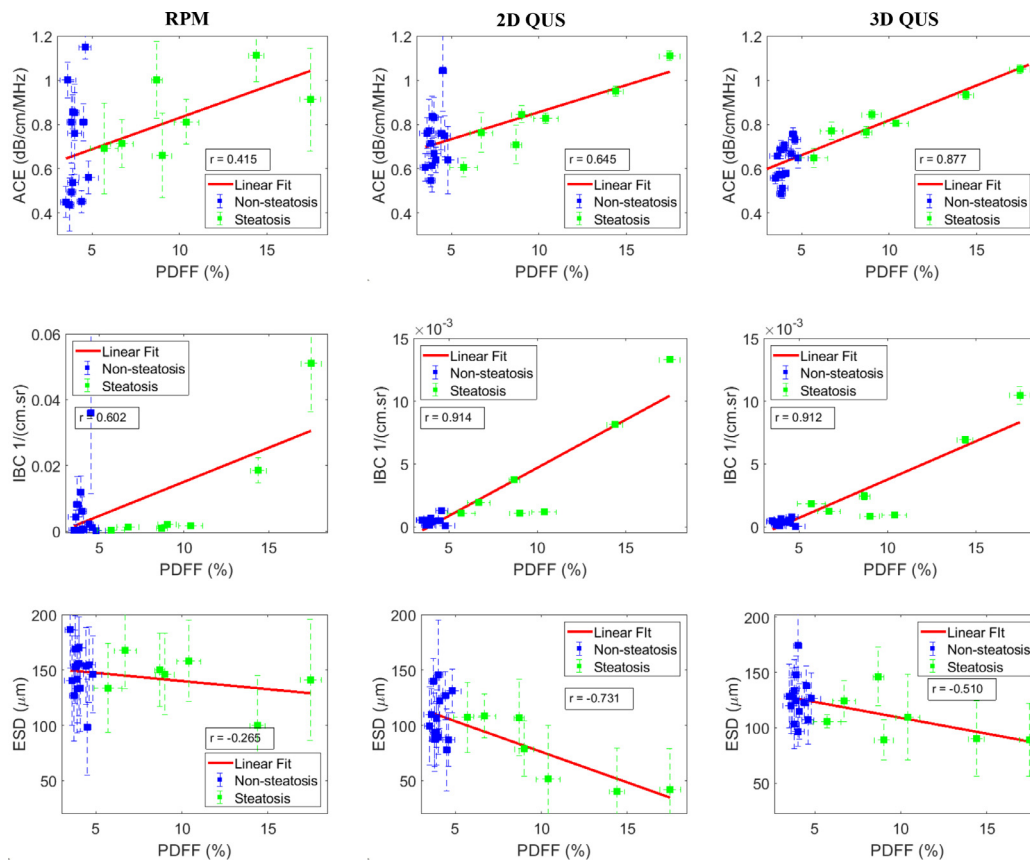


Fig. 11. *In vivo* human liver QUS measures from twenty-one patients and their correlation with proton density fat fraction. The vertical and horizontal error bars show the standard deviation in QUS measure and PDFF measure, respectively, whereas the square represents the mean calculated over a region-of-interest.

Table 4
Steatosis classification results for different QUS feature combination.

Features	Accuracy			AUROC			p - value
	RPM	2D QUS	3D QUS	RPM	2D QUS	3D QUS	
ACE	0.62	0.71	0.95	0.70	0.68	0.93	0.01
IBC	0.67	0.81	0.95	0.40	0.97	1.00	0.37
ESD	0.67	0.81	0.76	0.53	0.75	0.76	0.94
ACE & IBC	0.67	0.81	0.95	0.72	0.97	1.00	0.37
IBC & ESD	0.57	0.81	0.86	0.77	0.85	0.93	0.71
ACE & ESD	0.67	0.81	0.95	0.52	0.97	1.00	0.48
ACE & IBC & ESD	0.76	0.86	1.00	0.70	0.97	1.00	0.48

phantom (phantom 2), as can be seen in Figs. 3 and 4. 2D adaptive QUS also show similar results for phantom 1 and phantom 2. With a similar scatterer properties (including IBC and ESD), the ΔSNR_{min}^{env} values of both of these phantoms remain below ΔSNR_{min}^{env} , with little effect of spatial weighting. Therefore, the uniform QUS and the weighted QUS methods are essentially similar when the tissue under experiment is homogeneous in terms of backscatter properties. The 3D QUS and 2D adaptive QUS method outperform the 2D QUS when the underlying tissue has variable backscatter properties, as is the case of phantom 3. Fig. 4 shows that the ΔSNR^{env} map was able to identify the boundaries where backscatter properties vary. Incorporating the ΔSNR^{env} information in the 3D QUS (as well as in 2D adaptive QUS) enables adaptive regularization, and therefore results in more accurate reconstruction of the ACE and IBC map compared to the uniform regularization in 2D QUS. It should be noted that both the RPM and the 2D QUS method exhibit an underestimation and an overestimation of ACE centring the boundary between medium with different backscatter properties, a trend

described in previous literature (Pawlicki and O'Brien, 2013; Deeba et al., 2019b). Both 3D QUS and 2D adaptive QUS method were able to overcome the issue. Additionally, the 3D regularization in 3D QUS further improves the QUS estimation quality compared to the 2D adaptive QUS, yielding accurate ACE and IBC results with close agreement to the values reported by the manufacturer.

For ESD computation, a Gaussian form factor has been used as it can successfully model the scattering properties of many soft tissues, including liver (Nguyen et al., 2019; Insana et al., 1990a). However, a spherical shell form factor is more appropriate for spherical glass beads, as were used in the phantoms in our experiments (Insana and Hall, 1990; Insana et al., 1990a). The Gaussian form factor would consistently overestimate the sphere size, resulting in an effective diameter greater than the physical diameter (Insana and Hall, 1990; Liu et al., 2010). The effective diameter of the glass beads can be found by comparing the Gaussian form factor to the spherical shell form factor and computing the conversion factor for the particular physical diameter within the us-

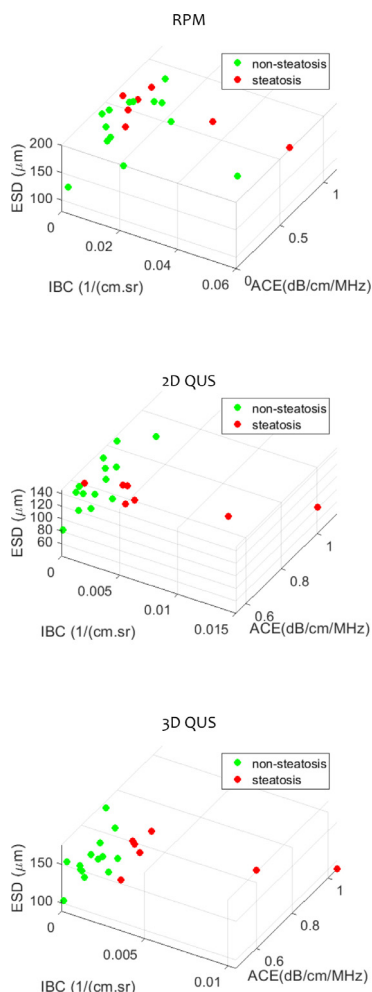


Fig. 12. Scatter plot of QUS measures representing normal and steatosis cases.

able frequency range (Liu et al., 2010). The physical diameters for inclusion 1, inclusion 3 and the background medium in phantom 3 are: 220 μm, 120 μm, 40 μm, and 70 μm, respectively. With conversion factors 1.27, 1.31, 1.56, and 1.28, respectively, the effective diameters have been found to be : 342, 158, 51, and 90 μm. The accuracy of ESD estimation depends on the estimation accuracy of the backscatter parameter, n . Therefore, the accurate backscatter parameter estimation obtained by the 3D QUS further is translated to accurate ESD estimation as can be seen in Fig. 5.

The CIRS phantom was specifically designed to cover the wide range of QUS parameters to be expected in human liver in vivo with different stage of steatosis. the 2D QUS method and the 3D QUS method both reach close to the ground truth value with high precision for the entire range of ACE from 0.37 to 1.18 dB/cm/MHz. The accuracy and precision of ESD estimation further depends on the range of ka_{eff} , the product of the wave number k and the effective scatterer radius a_{eff} , which should be within 0.5 to 1.2 for optimum results (Insana et al., 1990a). For the frequency range of 2 MHz to 3.5 MHz used in our experiments, the ka_{eff} values for the scatterers in inclusion 1, 2, 3 and the background are: 1.40–2.44, 0.64–1.13, 0.21–0.36, and 0.37–0.64, respectively. Accordingly, we obtain high estimation error and variance for inclusion 1 and 3, as the corresponding ka_{eff} values are well outside of the optimal range. The high variance in the ESD estimation for background scatterers can partly be attributed to the boundary artifacts. Finally, the ka_{eff} for the scatterers in inclusion 2 is within the optimal

range, resulting in an accurate and precise ESD estimation (Fig. 5, Fig. 6c and Table 3).

The advantage of using spatial weighting in the proposed 3D QUS over the uniform QUS and the baseline RPM is further evident from the CNR study. The 3D QUS improves the contrast significantly for all three QUS parameters compared to the 2D QUS and baseline RPM. This improved CNR would translate into better identification of abnormality in clinical application. The processing is done using a standard personal computer (Intel(R) Core(TM) i5-10210U CPU at 1.6 GHz with 16 GB RAM). The computation time for the proposed algorithm depends on the ROI size. For a volume-of-interest with lateral dimension of 35 scanlines, axial dimension of 6 cm (1450 samples or 122 λ) and elevational dimension of 5 planes, the computation time was 203.30 s. The bulk of the computation time (180.67 s) was used for computing power spectrum estimates, whereas the rest (22.6 s) was used for 3D TV regularization.

The proposed QUS method utilizes the volumetric RF data acquired by a motorized 3D transducer. The use of a 3D system allows the volumetric QUS reconstruction, using a three-dimensional total variation regularization. Fig. 8 shows that 3D regularization improves the estimation variance at a faster rate than the theoretical $1/\sqrt{N}$ curve obtained from averaging N uncorrelated realizations. The advantage of utilizing volumetric data could be further enhanced in case of in vivo liver data. The correlation between two radio-frequency signal data separated by ΔN planes, gives a measure of effectiveness of spatial compounding (Herd et al., 2012), where a low normalized correlation coefficient value (< 0.2) indicates independent data realizations. Fig. 9 shows that the radio-frequency data obtained from in vivo liver get decorrelated at a faster rate with the increasing plane separation compared to the one obtained from the phantom. As the ground truth values for QUS variance in in vivo liver is unknown, we cannot obtain the exact measures of improvement with increasing data realizations. Nevertheless, the improved decorrelation between subsequent planes is an effective indicator of improvement in QUS measurement for in vivo liver compared to phantom.

Our QUS estimation results for liver in vivo were comparable to the MRI-PDFP performance, the current gold standard. The presence of hepatic steatosis was defined as MRI-PDFP > 5% (Caussy et al., 2018). From the correlation analysis, it was found that the ACE and IBC obtained using the proposed method have strong positive association with MRI-PDFP, whereas the ESD was found to be negatively correlated to MRI-PDFP (Fig. 11). The ACE and IBC correlation results are in agreement with previous studies on human liver in vivo (Andre et al., 2014b; Tada et al., 2019), additionally with an improved correlation. On the other hand, this is the first work to report the correlation between ESD of human liver and MRI-PDFP. Nevertheless, previous studies on rabbit fatty liver found negative correlation between ESD and fat content of the liver (Nguyen et al., 2019). Using different combination of these three QUS parameters estimated using the proposed method with a simple QDA classifier, we were able to discriminate between the steatosis and the non-steatosis class with an accuracy up to 100% and area under the receiver operating characteristic (AUROC) of 1. Among the QUS features, ESD was least effective to classify the two groups. However, the high contrast achievable using ESD (Fig. 7) suggests that ESD, though exhibit inferior performance to identify steatosis which is a diffuse condition, might be effective in characterizing focal diseases.

Using Youden index, the optimal threshold for ACE, IBC and ESD to detect the presence of steatosis were found to be 0.77 dB/cm/mHz, $8.5e^{-4}$ 1/(sr.cm), and 146.3 μm. The ACE and IBC cut-off agree with the previous findings, where the ACE and IBC cut-off values were equal to 0.76 dB/cm/MHz and $2.7e^{-3}$ 1/(sr.cm) (Andre et al., 2014b). Among the limitations of our study is the

ESD values obtained for steatosis participants, which partially lie within non-optimal $ka_{eff} < 0.5$ range. Future work will involve application of comparatively higher frequency range to mitigate the problem. Also, we observe high variance in the ESD estimation for the liver study, which can be due to the presence of coherent component in the backscatter RF data. Therefore, we will further explore different signal decomposition techniques to separate the diffuse component from the coherent component (Nizam et al., 2020). Also, instead of using a Gaussian form factor, tissue-specific form factors can be derived from the impedance maps of underlying tissue and could be used for improved ESD computation (Mamou et al., 2005). Another limitation of the in vivo liver study is that the MRI-PDFF images and the ultrasound images are not registered. Though care has been taken to ensure that the planes-of-interest in MRI and ultrasound roughly coincide, a registration scheme would allow direct comparison with possible identification of focal lesions. Finally, we have demonstrated through phantom studies that the proposed method is able to attain improved reconstruction of QUS parameters for heterogeneous regions-of-interest. However, validation of current study is limited to in vivo liver, which involves large homogeneous parenchyma. Further studies are required for validating the efficacy of the proposed method for heterogeneous and thin tissue, such as the placenta, kidney and dermis.

5. Conclusion

In this paper, we present a multiparametric 3D weighted QUS method, which simultaneously measures three biomarkers for tissue characterization including ACE, IBC and ESD. The method incorporating a spatially adaptive regularization was able to achieve improved precision-resolution trade-off in QUS reconstruction in the presence of underlying tissue homogeneity. The three-dimensional regularization further improves the QUS estimation precision with a standard deviation reduction faster than the theoretical $1/\sqrt{N}$ rate achievable by averaging of N uncorrelated realizations. With strong correlation to the current gold standard MRI-PDFF, each of the three parameters demonstrate the potential to detect hepatic steatosis. The combination of the QUS parameters further improve the steatosis classification performance. The proposed volumetric QUS method therefore promises a comprehensive assessment tool for non-alcoholic fatty liver disease.

Declaration of Competing Interest

The authors declare that they have no known competing financial interests or personal relationships that could have appeared to influence the work reported in this paper.

CRediT authorship contribution statement

Farah Deeba: Conceptualization, Methodology, Software, Validation, Formal analysis, Writing – original draft, Visualization. **Caitlin Schneider:** Conceptualization, Investigation, Resources, Data curation, Writing – review & editing. **Shahed Mohammed:** Software, Validation, Writing – review & editing. **Mohammad Honarvar:** Software, Investigation, Resources, Data curation. **Julio Lobo:** Software, Investigation, Resources, Data curation, Writing – review & editing. **Edward Tam:** Resources. **Septimiu Salcudean:** Conceptualization, Writing – review & editing, Supervision, Project administration, Funding acquisition. **Robert Rohling:** Conceptualization, Writing – review & editing, Supervision, Project administration, Funding acquisition.

Acknowledgments

The authors would like to thank the support from the Charles A. Laszlo Chair in Biomedical Engineering held by Professor Salcudean, Microsoft corporation, Schlumberger foundation, Canadian Institutes of Health Research (CIHR) : MOP-142439 and the Natural Sciences and Engineering Research Council of Canada (NSERC): CRDPJ 537496-18. NSERC CIHR Collaborative Health Research Project: FAS F15-04456.

References

- Andre, M.P., Han, A., Heba, E., Hooker, J., Loomba, R., Sirlin, C.B., Erdman, J.W., O'Brien, W.D., 2014. Accurate diagnosis of nonalcoholic fatty liver disease in human participants via quantitative ultrasound. In: 2014 IEEE International Ultrasonics Symposium, pp. 2375–2377.
- Andre, M.P., Han, A., Heba, E., Hooker, J., Loomba, R., Sirlin, C.B., Erdman, J.W., O'Brien, W.D., 2014. Accurate diagnosis of nonalcoholic fatty liver disease in human participants via quantitative ultrasound. IEEE, pp. 2375–2377.
- Bamber, J.C., Hill, C.R., 1981. Acoustic properties of normal and cancerous human liver-I. Dependence on pathological condition. *Ultrasound Med. Biol.* 7 (2), 121–133.
- Causy, C., Alquiraish, M.H., Nguyen, P., Hernandez, C., Cepin, S., Fortney, L.E., Ajmera, V., Bettencourt, R., Collier, S., Hooker, J., et al., 2018. Optimal threshold of controlled attenuation parameter with MRI-PDFF as the gold standard for the detection of hepatic steatosis. *Hepatology* 67 (4), 1348–1359.
- Coila, A.L., Lavarello, R., 2017. Regularized spectral log difference technique for ultrasonic attenuation imaging. *IEEE Trans. Ultrason., Ferroelectr. Freq. Control* 65 (3), 378–389.
- Coleman, D.J., Lizzi, F.L., Insana, M.F., 1983. Computerized ultrasonic tissue characterization of ocular tumors. *Am. J. Ophthalmol.* 96 (2), 165–175.
- Deeba, F., Ma, M., Pesteie, M., Terry, J., Pugash, D., Hutcheon, J.A., Mayer, C., Salcudean, S., Rohling, R., 2019. Attenuation coefficient estimation of normal placentas. *Ultrasound Med. Biol.* 45 (5), 29–31.
- Deeba, F., Schneider, C., Mohammed, S., Honarvar, M., Tam, E., Salcudean, S., Rohling, R., 2019. Swtv-ace: spatially weighted regularization based attenuation coefficient estimation method for hepatic steatosis detection. In: International Conference on Medical Image Computing and Computer-Assisted Intervention, pp. 610–618.
- DeLong, E.R., DeLong, D.M., Clarke-Pearson, D.L., 1988. Comparing the areas under two or more correlated receiver operating characteristic curves: a nonparametric approach. *Biometrics* 44, 837–845.
- Feleppa, E.J., Mamou, J., Porter, C.R., Machi, J., 2011. Quantitative ultrasound in cancer imaging. In: *Seminars in Oncology*. Elsevier, pp. 136–150.
- Feltovich, H., Hall, T.J., Berghella, V., 2012. Beyond cervical length: emerging technologies for assessing the pregnant cervix. *Am. J. Obstet. Gynecol.* 207 (5), 345–354.
- Fujiwara, Y., Kuroda, H., Abe, T., Ishida, K., Oguri, T., Noguchi, S., Sugai, T., Kamiyama, N., Takikawa, Y., 2018. The b-mode image-guided ultrasound attenuation parameter accurately detects hepatic steatosis in chronic liver disease. *Ultrasound Med. Biol.* 44 (11), 2223–2232.
- Gerig, A., Chen, Q., Zagzebski, J., Varghese, T., 2004. Correlation of ultrasonic scatterer size estimates for the statistical analysis and optimization of angular compounding. *J. Acoust. Soc. Am.* 116 (3), 1832–1841.
- Goodman, J.W., 1985. *Wiley series in pure and applied optics. Statistical Optics*. Wiley, New York.
- Grant, M., Boyd, S., Ye, Y., 2009. *Cvx: Matlab software for disciplined convex programming*.
- Guerrero, Q.W., Feltovich, H., Rosado-Mendez, I.M., Carlson, L.C., Li, G., Hall, T.J., 2018. Anisotropy and spatial heterogeneity in quantitative ultrasound parameters: relevance to the study of the human cervix. *Ultrasound Med. Biol.* 44 (7), 1493–1503.
- Herd, M.-T., Hall, T.J., Jiang, J., Zagzebski, J.A., 2012. Improving the statistics of quantitative ultrasound techniques with deformation compounding: an experimental study. *Ultrasound Med. Biol.* 37 (12), 2066–2074.
- Insana, M.F., Hall, T.J., 1990. Parametric ultrasound imaging from backscatter coefficient measurements: image formation and interpretation. *Ultrason. Imaging* 12 (4), 245–267.
- Insana, M.F., Wagner, R.F., Brown, D.G., Hall, T.J., 1990. Describing small-scale structure in random media using pulse-echo ultrasound. *J. Acoust. Soc. Am.* 87 (1), 179–192. doi:10.3174/ajnr.A1256.Functional.
- Insana, M.F., Wagner, R.F., Brown, D.G., Hall, T.J., 1990. Describing small-scale structure in random media using pulse-echo ultrasound. *J. Acoust. Soc. Am.* 87 (1), 179–192.
- Jensen, J.A., 1996. Field: A program for simulating ultrasound systems. In: 10th Nordic/Baltic Conference on Biomedical Imaging, Vol. 4, Supplement 1, Part 1, pp. 351–353.
- Kanayama, Y., Kamiyama, N., Maruyama, K., Sumino, Y., 2013. Real-time ultrasound attenuation imaging of diffuse fatty liver disease. *Ultrasound Med. Biol.* 39 (4), 692–705. doi:10.1016/j.ultrasmedbio.2012.10.021.
- Laugier, P., Haïat, G., 2011. *Bone Quantitative Ultrasound*, 576. Springer.

- Li, P.-C., O'Donnell, M., 1994. Evaluational spatial compounding. *Ultrason. Imaging* 16 (3), 176–189.
- Lin, S.C., Heba, E., Wolfson, T., Ang, B., Gamst, A., Han, A., Erdman Jr., J.W., O'Brien Jr., W.D., Andre, M.P., Sirlin, C.B., et al., 2015. Noninvasive diagnosis of nonalcoholic fatty liver disease and quantification of liver fat using a new quantitative ultrasound technique. *Clin. Gastroenterol. Hepatol.* 13 (7), 1337–1345.
- Liu, W., Zagzebski, J.A., Liu, W., 2010. Trade-offs in data acquisition and processing parameters for backscatter and scatterer size estimations. *IEEE Trans. Ultrason., Ferroelectr. Freq. Control* 57 (2), 340–352. doi:10.1109/TUFFC.2010.1414.
- Loomba, R., Sanyal, A.J., 2013. The global NAFLD epidemic. *Nat. Rev. Gastroenterol. Hepatol.* 10 (11), 686–690.
- Mamou, J., Oelze, M.L., 2013. *Quantitative Ultrasound in Soft Tissues*. Springer doi:10.1007/978-94-007-6952-6.
- Mamou, J., Oelze, M.L., O'Brien Jr., W.D., Zachary, J.F., 2005. Identifying ultrasonic scattering sites from three-dimensional impedance maps. *J. Acoust. Soc. Am.* 117 (1), 413–423.
- Mashhood, A., Raikar, R., Yokoo, T., Levin, Y., Clark, L., Fox-Bosetti, S., Middleton, M.S., Riek, J., Kauh, E., Dardzinski, B.J., et al., 2013. Reproducibility of hepatic fat fraction measurement by magnetic resonance imaging. *J. Magn. Reson. Imaging* 37 (6), 1359–1370.
- McFarlin, B.L., Balash, J., Kumar, V., Bigelow, T.A., Pombar, X., Abramowicz, J.S., O'Brien, W.D., 2015. Development of an ultrasonic method to detect cervical remodeling in vivo in full-term pregnant women. *Ultrasound Med. Biol.* 41 (9), 2533–2539. doi:10.1016/j.ultrasmedbio.2015.04.022.
- Nam, K., Zagzebski, J.A., Hall, T.J., 2013. Quantitative assessment of in vivo breast masses using ultrasound attenuation and backscatter. *Ultrason. Imaging* 35 (2), 146–161. doi:10.1177/0161734613480281.
- Nguyen, T.N., Podkova, A.S., Tam, A.Y., Arnold, E.C., Miller, R.J., Park, T.H., Do, M.N., Oelze, M.L., 2019. Characterizing fatty liver in vivo in rabbits, using quantitative ultrasound. *Ultrasound Med. Biol.* 45 (8), 2049–2062.
- Nizam, N.I., Ara, S.R., Hasan, M.K., 2020. Classification of breast lesions using quantitative ultrasound biomarkers. *Biomed. Signal Process. Control* 57, 101786.
- Noureddin, M., Lam, J., Peterson, M.R., Middleton, M., Hamilton, G., Le, T.-A., Betten-court, R., Changchien, C., Brenner, D.A., Sirlin, C., et al., 2013. Utility of magnetic resonance imaging versus histology for quantifying changes in liver fat in non-alcoholic fatty liver disease trials. *Hepatology* 58 (6), 1930–1940.
- Oelze, M.L., Mamou, J., 2016. Review of quantitative ultrasound: envelope statistics and backscatter coefficient imaging and contributions to diagnostic ultrasound. *IEEE Trans. Ultrason., Ferroelectr. Freq. Control* 63 (2), 336–351. doi:10.1109/TUFFC.2015.2513958.
- Oelze, M.L., O'Brien, W.D., 2004. Defining optimal axial and lateral resolution for estimating scatterer properties from volumes using ultrasound backscatter. *J. Acoust. Soc. Am.* 115 (6), 3226–3234. doi:10.1121/1.1739484.
- Oelze, M.L., Zachary, J.F., O'Brien Jr., W.D., 2002. Characterization of tissue microstructure using ultrasonic backscatter: theory and technique for optimization using a Gaussian form factor. *J. Acoust. Soc. Am.* 112 (3), 1202–1211.
- Pawlicki, A.D., O'Brien Jr., W.D., 2013. Method for estimating total attenuation from a spatial map of attenuation slope for quantitative ultrasound imaging. *Ultrason. Imaging* 35 (2), 162–172.
- Pohlhammer, J.D., O'Brien, W.D., 1980. *Medical physics of CT and ultrasound: Tissue imaging and characterization*, Vol. 6. The American Institute of Physics New York.
- Rau, R., Unal, O., Schweizer, D., Vishnevskiy, V., Goksel, O., 2020. Frequency-dependent attenuation reconstruction with an acoustic reflector. arXiv preprint arXiv:2003.05658.
- Rohrbach, D., Wodlinger, B., Wen, J., Mamou, J., Feleppa, E., 2018. High-frequency quantitative ultrasound for imaging prostate cancer using a novel micro-ultrasound scanner. *Ultrasound Med. Biol.* 44 (7), 1341–1354.
- Rosado-Mendez, I.M., Nam, K., Hall, T.J., Zagzebski, J.A., 2013. Task-oriented comparison of power spectral density estimation methods for quantifying acoustic attenuation in diagnostic ultrasound using a reference phantom method. *Ultrason. Imaging* 35 (3), 214–234.
- Rubert, N., Varghese, T., 2014. Scatterer number density considerations in reference phantom-based attenuation estimation. *Ultrasound Med. Biol.* 40 (7), 1680–1696.
- Rudin, L.I., Osher, S., Fatemi, E., 1992. Nonlinear total variation based noise removal algorithms. *Phys. D* 60 (1–4), 259–268.
- Tada, T., Kumada, T., Toyoda, H., Kobayashi, N., Sone, Y., Oguri, T., Kamiyama, N., 2019. Utility of attenuation coefficient measurement using an ultrasound-guided attenuation parameter for evaluation of hepatic steatosis: comparison with MRI-determined proton density fat fraction. *Am. J. Roentgenol.* 212 (2), 332–341.
- Treese, G., Prager, R., Gee, A., 2005. Ultrasound attenuation measurement in the presence of scatterer variation for reduction of shadowing and enhancement. *IEEE Trans. Ultrason., Ferroelectr. Freq. Control* 52 (12), 2346–2360.
- Vajih, Z., Rosado-Mendez, I.M., Hall, T.J., Rivaz, H., 2018. Low variance estimation of backscatter quantitative ultrasound parameters using dynamic programming. *IEEE Trans. Ultrason., Ferroelectr. Freq. Control* 65 (11), 2042–2053.
- Wear, K.A., 2002. *IEEE Trans. Ultrason., Ferroelectr. Freq. Control* 49 (11), 1572–1582.
- Wear, K.A., Stiles, T.A., Frank, G.R., Madsen, E.L., Cheng, F., Feleppa, E.J., Hall, C.S., Kim, B.S., Lee, P., O'Brien Jr., W.D., et al., 2005. Interlaboratory comparison of ultrasonic backscatter coefficient measurements from 2 to 9 MHz. *J. Ultrasound Med.* 24 (9), 1235–1250.
- Welch, P.D., 1967. The use of fast Fourier transform for the estimation of power spectra: a method based on time averaging over short, modified periodograms. *IEEE Trans. Audio Electroacoust.* 15 (2), 70–73.
- Wong, V.W.-S., Petta, S., Hiriart, J.-B., Cammà, C., Wong, G.L.-H., Marra, F., Vergniol, J., Chan, A.W.-H., Tuttolomondo, A., Merrouche, W., et al., 2017. Validity criteria for the diagnosis of fatty liver by m probe-based controlled attenuation parameter. *J. Hepatol.* 67 (3), 577–584.
- Yao, L.X., Zagzebski, J.A., Madsen, E.L., 1990. Backscatter coefficient measurements using a reference phantom to extract depth-dependent instrumentation factors. *Ultrason. Imaging* 12 (1), 58–70.